Laser ignition of *iso*-octane jets under compression-ignition conditions

Guanxiong Zhai[a], Sensen Xing[a], Paul R. Medwell [b], Anthony C.Y. Yuen [a], Sanghoon Kook[a], Guan Heng Yeoh[a], Qing Nian Chan[a,*]

School of Mechanical and Manufacturing Engineering, University of New South Wales, Sydney, NSW 2052, Australia

School of Mechanical Engineering, The University of Adelaide, Adelaide, SA 5005, Australia

Abstract

This work aims to investigate the effect of laser-induced plasma ignition (LI) on combustion behaviours of *iso*-octane (a gasoline surrogate) at compression-ignition (CI) conditions. A high-energy laser was used to force the fuel ignition at a quiescent-steady environment inside an optically accessible constant-volume combustion chamber with 900 K ambient gas temperature, 22.8 kg/m^3 ambient gas density and 21 vol.% O_2 concentration. A diesel surrogate (*n*-heptane) was tested at a lower charge temperature of 735 K to offset the fuel reactivity, such that the flame has a similar lift-off length compared to the *iso*-octane flame. Forced laser ignition was introduced either before or after the natural autoignition fuels, at axial locations 15 mm and 30 mm from the nozzle, for both fuel jets. High-speed schlieren imaging, heat release analysis and flame luminosity measurement were applied to the flames. The high-speed schlieren imaging was used to monitor the flame structure evolution of the natural ignition and LI cases. The temporal evolution of the flame lift-off lengths show that the uncertainties in the lift-off distances of the natural autoignition events can be reduced by more than 80% after LI. The laser-affected flame lift-off lengths shift towards the natural lift-off distances after LI. The uncertainties in the lift-off lengths also increase, as the flame stabilisation locations approach the natural lift-off distances. Under the test conditions of this work, the rates at which the *iso*-octane flames shift downstream are faster than the *n*-heptane cases. The heat release rate profiles show high heat release from the flames following the LI events, before transitioning to lower steady values. The flame luminosity measurements indicate increased soot formation with the jets following the LI events. The luminosity levels, however, decrease as the flame lift-off distances shift downstream from their initial forced ignition locations over time.

Keywords: Gasoline compression-ignition, Constant-volume combustion chamber, Laser-induced plasma ignition, Flame evolution, Flame stabilisation

*Corresponding author: qing.chan@unsw.edu.au

1. Introduction

Low-temperature combustion is an advanced combustion concept that shows promise in reducing both soot and NO_x emissions while maintaining or even increasing the performance of the CI engine. [1–3]. Among the various low-temperature combustion concepts proposed, gasoline compression ignition (GCI) is one of the closest to conventional CI engine configuration. The main difference lies in the use of less reactive fuels, such as gasoline, instead of diesel [4, 5]. The concept of GCI lies in the forming of overall lean, premixed charge before ignition, to help suppress soot and NO_x formation [6–8], which have been shown to have direct and indirect effects on human health [9–11]. Previous studies have shown that GCI engines are capable of meeting the stringent emission regulations with exhaust after-treatment system while maintaining high engine efficiencies for a wide range of operation conditions [4, 8, 12–17].

Despite the potential of GCI, further improvements are required to improve the combustion stability of GCI engines under cold-start and low-load operating conditions [4, 16, 18, 19]. For example, previous studies have shown that the operation of stratified GCI engines that were fuelled using conventional gasoline blends can become unstable at low engine loads (*e.g.*, at engine loads lower than 5 bar indicated mean effective pressure-gross) or idle [17, 19]. There have been several attempts to extend the low-load limit of the GCI engine, including the testing of different injection and thermal management strategies, such as multiple injections, negative valve overlapping and exhaust re-breathing valve technologies [18]. The ignition and combustion processes of these different approaches, nonetheless, still depend on the reactivity of the mixture used. The effectiveness of these alternative strategies is also susceptible to changing engine operating parameters, such as increased engine speed, and can be challenging to implement in certain engine configurations, such as small-bore engines. In the former, increasing engine speed will reduce the allowable time for stable ignition. In the case of the latter, the heat from the exhaust gases of the small-bore engine may not be sufficient to meaningfully extend the stability of the engine operating range [7, 20]. A promising alternative to extending the operating range of the GCI engine is to combine it with a separate ignition source, such as a spark plug and glow plug, to assist with the ignition and combustion processes. Previous studies have reported the effectiveness of this method to extend the ignition stability to low-load operating conditions [21–23]. It is noteworthy that Mazda now implements the spark-assisted ignition approach in their Skyactive-X 2.0L engine for GCI combustion under low-load and idle conditions [5, 24].

In order to further improve the ignition and combustion stability of GCI, different ignition strategies, such as laser-induced spark ignition, which has attributes that are favourable towards improved ignition, kernel development and flame propagation over conventional electric spark systems, are subjects of interest [20, 25–28]. Laser spark ignition, which is also known as laser-induced plasma ignition, involves using laser irradiance in the order of 10^{10}–10^{11} W/cm^3

[29–31], to produce a spark plasma via multi-photon ionisation and electron cascade processes. To implement laser spark ignition, the focusing of pulsed laser beams into a small spot diameter, typically to the order of micrometres [30, 31], is often used to ensure sufficient irradiance is generated. Compared with conventional electric spark systems, laser-induced spark ignition has the added advantages of being able to target any arbitrary location within the engine cylinder—a feature that has been used to provide better control of flame propagation distance and combustion duration based on engine speed and load conditions [20, 26, 32]. The laser spark ignition is also capable of igniting leaner mixture, which can lead to lower combustion temperature and hence, NO_x formation [20, 25, 26, 28]. The laser-induced spark ignition system also has the advantage of being able to avoid the quenching of the initial flame kernel, which can occur with a spark plug ignition system due to the heat loss to its electrodes [26, 29, 32]. The lifespan and ignition time precision of laser-induced ignition, in principle, can also exceed those of a conventional spark-plug ignition system [26, 28, 32]. Laser spark ignition system, therefore, has the potential to facilitate further improvement in efficiency, the extension of operation range and reduction in pollutant emissions in GCI engines [26], if its advantages can be fully realised in practical settings.

Laser-induced spark ignition has been previously tested in performance engines and other combustion vessels for a range of fuels, including methane, hydrogen and diesel, with the results indicating that the laser-induced sparks can improve some combustion characteristics, compared with conventional spark systems [27–30, 32, 33]. For gasoline-like fuels, Mullett *et al.* [34] have previously studied the effects of beam energy and quality from a Q-switched Nd:YAG laser (1064 nm) on the control of laser ignition in a 4-cylinder engine under homogeneous stoichiometric gasoline-air charge. They observed better combustion performance (as measured from the coefficient of variation of the indicated measure effective pressure) and stability (as deduced from the peak pressure cycle-to-cycle variation) with a laser-induced spark when compared with an electric spark. Their study also shown that the laser energy used has a greater impact on the ignition stability of their system, comparing with the quality of the beam used [34]. In a separate study, Xu *et al.* [35] studied the probability of laser-spark ignition as well as the required minimum ignition energy for premixed gasoline–air mixtures. In their study, which was performed in a constant-volume combustion chamber (CVCC) and laser ignition was accomplished using a 532 nm or 1064 nm beam from a Q-switched Nd:YAG laser, it was observed that the overall ignition probability increases with higher laser energy. Their study also reported that the minimum required ignition energy displayed a parabolic shape trend over a range of equivalence ratios, from 0.7 to 1.7, with a local minimum observed at the approximately stoichiometric ratio for both tested laser wavelengths [35]. Weinrotter *et al.* tested a fuel consisting of 80% *iso*-octane (gasoline surrogate) and 20% *n*-heptane at homogeneous charge compression (HCCI) combustion mode in an optical engine with a laser spark ignition system. Their study demonstrated that laser spark plasma ignition can be used to change the initial ignition location, comparing

with unsupported HCCI combustion mode. Pastor *et al.* [36] recently tested the laser-spark ignition approach in a single-cylinder optically accessible engine, which was fuelled by two fuel blends comprising of 50 vol.% and 70 vol.% commercial gasoline with diesel. In their study, it was demonstrated that laser spark ignition can be used to change the ignition delay and lift-off length of the flames. It was also demonstrated that with a proper ignition system configuration, the combustion characteristics of the less reactive gasoline-diesel blends can be controlled to become similar to that of pure diesel, leading to a similar energy release rate and combustion efficiency, but with less soot formation.

With all of the findings from previous studies considered, this work seeks to extend the fundamental understanding of the combustion behaviour of the gasoline-like fuel as a function of the local conditions of the laser ignition site. For this work, a high-energy laser was focused to generate a plasma at specific spatial locations and times after the start of injection (aSOI) of gasoline surrogate jets (*i.e.*, *iso*-octane) in an optically accessible CVCC. This work is focused on monitoring the transient ignition and combustion characteristics of the reacting gasoline-like jets in the presence and absence of laser spark induced ignition, under GCI engine relevant conditions, which the previous GCI laser spark ignition studies devoted less focus to. Through these parametric variations, further insights into the fundamental mechanisms associated with the local conditions of the fuels at the ignition locations can affect the ignition and combustion characteristics of the laser-perturbed jet flames can be attained, in comparison to the natural autoignition cases. Furthermore, this work also aims to directly compare the application of the laser-induced spark ignition technique to a diesel surrogate (*i.e.*, *n*-heptane) jet at similar laser ignition locations and timings. Considering that the effects of the local conditions on the ignition and combustion characteristics of the laser-perturbed jets are of interest to this work, an effort is made to change the charge conditions that the fuels are subjected to, and therefore, offset the differences in their fuel reactivity. This is to keep the lift-off lengths of the flames approximately the same within a comparison set, and hence, having similar fuel-air mixture distribution conditions at the laser ignition locations.

2. Experimental details

2.1. Constant-volume combustion chamber

Experiments were performed in an optically accessible constant-volume combustion chamber (CVCC) under simulated, quiescent CI engine conditions. The CVCC has a cubical chamber (114 mm per side) with six ports. To provide optical access, sapphire windows were installed at four sides of the chamber. A mixing fan, mounted at the top of CVCC, was used to ensure spatially uniform ambient temperature distribution within the chamber during the fuel injection events. For this work, the fuel sprays were directly injected into the chamber via an axially drilled

single-hole fuel injector with an orifice diameter of 105 μm, which was mounted onto one of the metal side ports. A schematic diagram of the CVCC with the diagnostic setups used is provided in Fig. 1.

Previous studies provide details about the procedure to simulate compression-ignition conditions (*e.g.*, [37–39]). To summarise, the chamber was initially filled to a specified density with a premixed, lean combustible charge that consisted of a mixture of C_2H_2, H_2, N_2 and O_2. The gas mixture was subsequently ignited by a spark plug to create a high temperature and pressure environment. For this study, the composition of the gas mixture was tailored to produce a targeted ambient O_2 gas concentration of 21 vol.% and 0 vol.% for the reactive and non-reactive cases, respectively, after the spark ignition. The ambient density was kept at 22.8 kg/m for all test cases. A piezoelectric pressure transducer (Kistler 6052C) was used to monitor the in-chamber pressure during the experiments. As the products of premixed combustion cooled down because of heat transfer to the vessel walls, the vessel pressure gradually decreased. The fuel spray was triggered to inject when the targeted chamber pressure was reached. Depending on the fuel type, the injector was triggered to inject once an ambient pressure condition of 5.2 MPa or 4.2 MPa, which corresponded to ambient gas temperatures of 900 K and 735 K, respectively, was reached. The ambient temperatures cited represent the core temperatures of the chamber, which were separately measured using a sheathed type-K thermocouple. For the chamber configuration used, a ratio of approximately 1.2 between the core and bulk temperatures was measured.

2.2. Fuel injection conditions

The fuels used for this work are *iso*-octane and *n*-heptane, to avoid the compositional complexity and variability that can arise from using commercial fuels [40]. The fuel injection pressures were controlled at 70 MPa, to produce an average steady injector flow rate of 2.53 kg/m^3. An extended long injection duration of 11.5 ms was used, to allow adequate time to monitor the transient responses of the jet flames to laser perturbations. A summary of the ambient and injection conditions are provided in Table. 1. *Iso*-octane and *n*-heptane are primary reference fuels (PRFs), which are commonly used as surrogates of gasoline and diesel for fundamental investigations, as they represent both ends of the octane rating scale [41]. Additionally, the *iso*-octane (*i.e.*, PRF100) and *n*-heptane (*i.e.*, PRF0) have similar overall physical properties (see Table 2), which can simplify their cross-comparisons. It is emphasised that these PRFs, however, do not fully replicate the actual chemical and physical properties of commercial gasoline and diesel fuels. Caution must, therefore, be exercised when attempting to interpret and extend the experimental results of this fundamental oriented work to actual engine operating conditions.

2.2.1. Laser-induced plasma ignition

The fundamental output from a 10 Hz pulsed Nd:YAG laser (Quantel Q-smart 450) was used to produce the spark plasma to force ignition. The laser beam with a beam diameter of 5 mm was first passed through a 3× expanding

telescope, which comprised of a Ø25 mm concave lens with a −100 mm focal length and a Ø250 mm convex lens with a 300 mm focal length, to expand its beam diameter into 15 mm. The beam expansion was used to produce a tight focal spot at the LI location. The expanded laser beam was then focused using a Ø25 mm convex lens with a 150 mm focal length to form a converging beam. The beam diameter at the focal point is estimated to be 37.9 µm by using the Eq. 1 [42]:

$$d = \frac{4M^2\lambda f}{\pi D}, \tag{1}$$

where d represents the beam diameters at the focal point, M represents the beam quality factor, which is estimated to be 1.67, λ represents the laser wavelength, π represents the circular constant, and D represents the beam diameter before the last focal lens. The laser energy at the focal point was measured to be 90 mJ/pulse using a digital power meter (Thorlabs PM100D). Based on the calculated beam waist, the area-averaged power at the focal point is approximately 0.9 W/mm^2. It is noted that the equation only provides a rough estimation of the beam diameter as it does not consider all optical effects, such as beam steering [42].

For the purpose of this work, there are several considerations when it comes to selecting the LI locations and timings. Firstly, the LI attempts should be performed at locations that are sufficiently separated from the natural lift-of lengths of the flames. This is to ensure there is adequate temporal and spatial interval to observe the characteristics of the subsequent flame development. Secondly, the testing of the LI efforts should ideally be tested in both fuel-rich and fuel-lean regions, as the state of the mixtures at the ignition locations are known to affect the flame behaviours [27]. Thirdly, the LI should be attempted at timings before and after the autoignition of the fuels. A previous study demonstrated that the combustion products formed during the premixed burn of jet flames can influence the flame behaviours throughout the remaining injection duration [43]. Evaluating the LI influence, in the presence and absence of the premixed-burn combustion products, is expected to provide more insights. Lastly, the LI should be attempted at locations that are downstream of the liquid phases of the fuels. This is to avoid the interaction between the evaporation and laser-induced combustion processes for the fuels, which can complicate the analysis of the results.

Using the lift-off length and ignition delay measurements from the natural autoignition cases, which will be later detailed in Section 3.2, the LI locations at 15 mm (*i.e.*, fuel-rich) and 30 mm (*i.e.*, fuel-lean) from nozzle along the jet axis, and LI timings ranging from 5.28–6.28 ms after the start of injection (aSOI) (*i.e.*, after autoignition) to 2.28 ms aSOI (*i.e.*, before autoignition) were selected for the test conditions of this work. It is noted LI timings of 5.28 ms aSOI and 6.28 ms aSOI were selected for the cases with LI after autoignition for PRF100 and PRF0, respectively, to ensure that the LI was attempted during the quasi-steady stabilisation periods of the flame jets. The test matrix with different LI locations and times are summarised in Table. 3. For the convenience of the discussion

presented in later sections, the test cases are systematically labelled to include information on the LI location and timing (see Table. 3).

2.3. Diagnostic techniques

The diagnostic techniques and their corresponding data processing approach used are discussed in this section. It is noted that measurements from at least 10 repetitions are used to calculate the ensemble-averaged results of the test cases presented in Section 3.

2.3.1. High-speed schlieren imaging

A 150 W Xenon arc lamp (Abet Technologies LS-150) was used to generate an approximately collimated beam. The light emission from the arc lamp was focused by a Ø50 mm plano-convex lens with a focal length of 75 mm, directed through a 2 mm aperture opening, before collimating using a Ø108 mm f/6 parabolic mirror. By using two Ø100 mm reflectors, the collimated beam was directed through the CVCC and onto a second parabolic mirror. A Ø5 mm aperture, placed at the focal point of the collimated beam, was used as a schlieren cut-off. The refocused beam was subsequently imaged using a high-speed CMOS camera (Photron SA-5), equipped with a 50 mm f/1.8 lens (Nikon-Nikkor). The camera was operated at a frame rate of 70 kHz with a 1 μs exposure time and an image resolution of 0.14 mm/pixel. The field-of-view (FoV) was restricted to 65 mm from the tip of the injector nozzle, to account for the camera settings used. Figure 1 presents the optical setup used for high-speed schlieren imaging.

2.3.2. Flame lift-off length derivation

Figure 2 presents the image processing procedures to derive the flame lift-off length information from its time-sequenced schlieren images. In brief, radial averaging was first performed at each axial location of each frame of a time-sequenced schlieren image. The single-row vector that the radial averaging process produced was then concatenated to produce a matrix, from which information about the jet combustion progress, such as ignition delay, lift-off length, and the temporal evolution of the flame structure can be derived. Figure 2 shows an example of a matrix that the image processing procedure can produce for a time-sequenced schlieren image series, which was recorded for a PRF100/15/5.28 test case. In the schlieren image, the fuel was injected from left to right. From the figure, it can be seen that the radial averaging and concatenation procedures make any part of the image that changes little from frame to frame, such as the background contrast in regions that are external to the jet, appears less distinct. This, in turn, helps to highlight the jet features within the image series that vary considerably over successive frames, such as the jet motion before ignition and the flame base position. In the case of the former, the jet motion produces a drift of small-scale structures in the background contrast behind the jet head. The radial averaging and concatenation

processes produce a recognisable curved profile in the resulting matrix (refer to the top right region of Matrix 'A' in Fig. 2). Similarly, the image processing method also makes the part of the image that the reacting jet, which typically has dark schlieren contrast, occupies appearing as a solid dark grey region in the resulting matrix. The variations allow the use of Otsu's thresholding method [44] to produce a binarised matrix see Matrix 'B' in Fig. 2), from which the edge of binarised region (shown as red solid lines in Fig. 2) can be used to derive lift-off length of the jet flame over time. The edge detection method is used to derive the results presented in Section 3.

2.3.3. Jet boundary detection

The jet boundaries were derived from the schlieren images, using a two-step approach that is based on a methodology described in Ref. [45]. In brief, a temporal-based standard deviation matrix was first computed for each image, by comparing it with the images immediately before and immediately after it from the same schlieren recording. Pixels with higher standard deviation values can be expected to locate at matrix region that corresponds to the intersection between the fast-moving jet and the comparatively stationary ambient gases. A filter was next used to sweep the matrix and connect the pixels with high intensities. Different jet properties, including the jet boundary and penetration, can subsequently be derived from the connected pixels.

2.3.4. Pressure and luminosity detection

The in-chamber pressure trace was measured by a piezoelectric pressure transducer (Kistler 6052C). The pressure traces were used to derive ignition delay and heat release rate using the approaches detailed in Sections 2.3.5 and 2.3.6, respectively. A sampling rate of 200 kHz was used for the pressure transducer.

A photodiode (Thorlabs PDA100A-EC), with a spectral sensitivity ranging from 340 to 1100 nm, was used to record the broadband luminosity change during the combustion events from the front window of the CVCC. The luminosity measurement can provide a qualitative indication of the difference in the soot formation in the fuel jets [43]. Depending on the luminosity level, the gain of the photodiode was adjusted accordingly to avoid signal saturation. A sampling rate of 200 kHz was also used for the photodiode.

2.3.5. Ignition delay derivation

As previously noted, the pressure within the CVCC continuously reduced because of convective heat loss through the chamber wall to the surroundings during the experiments. An exponential curve was used to estimate the pressure change within the chamber due to the heat loss effect only [46, 47]. By finding the difference between the actual measured and the fitted pressure values, the net pressure rise from the ignition and combustion of the fuel injection event only can be determined. For this work, a threshold that corresponded to 2% of the net pressure change was

set. This threshold value was found adequate to allow the detection of the start of the high-temperature combustion process while avoiding the interference from the noise in the pressure signal before the ignition process. For this work, the ignition delay is defined as the time instant when the corrected pressure reading exceeds this threshold.

2.3.6. Heat release derivation

Heat release rate (HRR) was calculated from the corrected pressure via:

$$\frac{\mathrm{d}Q}{\mathrm{d}t} = \frac{\gamma}{\gamma - 1} P \frac{\mathrm{d}V}{\mathrm{d}t} + \frac{1}{\gamma - 1} V \frac{\mathrm{d}P}{\mathrm{d}t} \tag{2}$$

where P represents the corrected pressure, V represents the volume of the combustion chamber. The γ represents the ratio of the specific heat, which is dependent on ambient temperature and is typically set as 1.3 [48]. The first term of the equation can be disregarded, considering that the volume of the CVCC is constant. The equation can, therefore, be simplified to:

$$\frac{\mathrm{d}Q}{\mathrm{d}t} = \frac{1}{\gamma - 1} V \frac{\mathrm{d}P}{\mathrm{d}t} \tag{3}$$

3. Results and discussion

3.1. Fuel-air mixing

To estimate the equivalence-ratio distributions within the jets at the experimental equations, a one-dimensional (1D) spray model, DICOM [49], was used. It is noted that a detailed verification of a 1D variable radial-profile model predictions with direct mixing measurements over a range of ambient densities, fuels, nozzle sizes, and nozzle shapes was performed in a previous study [50]. The study showed that by adjusting the global parameters of the model, such as jet penetration or jet spread angle that can be experimentally measured using typical line-of-sight diagnostics methods, the 1D model can generate mixture predictions of the vaporised sprays that are within the uncertainties of experimental measurements. For this work, all model parameters were kept the same as in the experiments and the spray cone angle was tuned to match the modelled and the experimental vapour penetration trends. A good agreement between the modelled and experimentally measured jet penetration trends for the fuels was found, when a spray cone angle of 32° was specified.

Figure 3 presents the experimentally measured and the simulated jet penetrations for the fuels. It is noted that the experimentally measured penetrations were derived from the schlieren images of the fuel jets when to non-reacting ambient conditions (*i.e.*, 0% oxygen concentration). The corresponding run-to-run uncertainties (± 1 standard devi-

ation) are also provided in the figure. From the figure, both fuels display comparable spray penetrations, which is expected, considering the similarities in the fluid properties [51, 52].

Figure 4 shows the steady-state equivalence ratio contours that the 1D model result of PRF100 estimated. The same mixture distribution can be expected for PRF0. An experimental jet contour, which was derived from a schlieren image of PRF100 jet at 5.28 ms aSOI (*i.e.*, when the jet can be expected to reach a quasi-steady state), is overlaid for comparison. The figure shows a good agreement between the very lean simulated contour (*i.e.*, ϕ=0.5) with the experimentally measured jet boundaries after the model cone angle was tuned based on the experimental jet penetration. The agreement provides some degree of confidence to the 1D simulation result. The model predicts that the equivalence ratios of 3.1 and 1.6 at the jet centre-line, at 15 mm and 30 mm from the nozzle, respectively. The corresponding cross-sectional averaged equivalence ratios at the axial locations are estimated to be 2.8 and 0.7. In a separate simulation (not shown), the model also shows similar equivalence ratios can be expected at the same LI locations at 2.28 ms aSOI, when the jet can be expected to be in a more transient state. The modelled equivalence ratios are used to interpret the experimental results under reactive conditions.

3.2. Natural autoignition cases

For reference purposes, the typical schlieren image sequences demonstrating the spray and combustion characteristics of PRF100 and PRF0 fuels are first presented in Fig. 5. It is noted that schlieren imaging is an optical technique that relies on the light deflection that occurs in the presence of refractive index gradients, which can be induced by the evaporative cooling, mixing and combustion processes of the fuel. The light deflection is then translated into intensity variation at the image plane. Depending on the refractive index difference between the mixture and its surrounding medium, the mixture on the image can assume a transparent or opaque appearance. Additionally, light scattering/absorption that occurs in the presence of the liquid jet can also lead to the darkening in the schlieren images [53, 54]. The image sequences in Fig 5. correspond to the conditions where the autoignition of the PRF100 and PRF0 fuels begin at 3.1 ms aSOI and 4.4 ms aSOI, respectively, and the lift-off stabilisation of the flames occur after. In each of the images, the fuel injects horizontally from left to right. The abscissa and ordinate of the axes indicate the axial and radial distances from the nozzle tip, respectively. Different time intervals are used for PRF100 and PRF0 jets to highlight the overall jet development stages that are most relevant for discussion. The time instant indicated on the top-left corner of each image panel indicates its time aSOI in milliseconds. Yellow dashed lines are used to indicate the minimum lift-off distances of the flames, when present. The minimum distances were derived using the methodologies described in Section 2.3.2.

High-speed schlieren is widely used to visualise both low- and high-temperature combustion processes in diesel studies [54–56]. Previous studies (*e.g.*, [56]) typically attributed the observed local softening in the schlieren effects

to the occurrence of low-temperature events. Specifically, the consumption of the fuel vapour may result in the release of intermediate species and modest heat, which may increase the local density and refractive index values to match that of the surrounding gases, such that the schlieren effects became less pronounced. For the studies that utilised different ambient gas temperatures, such as this work, using schlieren images to infer the occurrence of low-temperature combustion events is challenging. For example, at lower ambient temperatures, it is possible that the low-temperature combustion, if present, can heat the vapour jet to become hotter than the ambient gas temperature. This can lead to a darkening in the schlieren image, but not to the same degree as the high-temperature combustion. At higher ambient temperature conditions, the low-temperature combustion can heat the temperature of the vaporised fuel to become closer to the ambient gases, without far exceeding it. This can result in a softening in the schlieren contrast. For this work, the high-speed schlieren images are only used to detect the occurrence of high-temperature combustion processes in the jets and the jet boundaries. For the former, the high temperature and low-density regions that the high-temperature combustion processes produce will have refractive indexes that are considerably different to the surrounding gases. Abrupt darkening in the schlieren contrast that is sufficiently distinct and recognisable is expected. For the latter, a two-step image processing procedure, which is independent of the schlieren contrast (see Section 2.3.3), was used to derive the jet boundaries.

The schlieren image sequence of the PRF100 case (left column, Fig 5) shows the first appearance of a region with dark schlieren contrast at about 2.94 ms aSOI. At 3.04 ms aSOI, the schlieren signal noticeably increases in contrast in several regions across the jet head, as seen in the image region downstream of 55 mm. At 4.09 ms aSOI, the darkened regions appear to grow/merge/overlap and cover the whole head of the jet, before displaying near-steady lift-off behaviour. There are two time instants (*i.e.*, 4.07 ms aSOI and 7.51 ms aSOI) in the image sequence when dark schlieren contrast regions spontaneously form upstream from the main flame body (annotated with red arrows in the left column of Fig 5). These darkened regions proceed to grow in size and eventually merge with the zone with the dark schlieren contrast downstream. These merging events lead to rapid decreases in the calculated lift-off distances. The evolution of the schlieren signal for the PRF0 case (right column, Fig 5) shows the first appearance of the dark schlieren contrast region at about 4.01 ms aSOI. In the previous studies, the isolated self-ignition events that occurred during the quasi-steady combustion period are reported to lead to an initial rapid decrease in the flame base positions, before reverting to their more natural lift-off locations. Compared with this work, the flame base fluctuations in the previous studies are of smaller magnitudes (*e.g.*, approximately ±2 mm in Refs. [42, 43], under the test conditions of their studies). For this work, the flame base of the PRF100 fuel can vary by more than 15 mm from its initial stabilisation location, as the schlieren images of 4.01–10.54 ms aSOI in Fig. 5 (left) shows. Compared with the PRF100 case, the initial increase in the schlieren signal is comparatively more uniform across a larger portion

of the jet centre, as seen in the schlieren images of 4.01–4.40 ms aSOI, downstream of 45 mm. The schlieren signal remains weak until about 4.69 ms aSOI, when it considerably darkens. For the PRF0 case, unlike PRF100, there is no clear instance when a region with a dark appearance that appears detached from the main flame body downstream can be identified. The spontaneous formation of flame kernels at locations that were upstream from the main flame bodies are also documented in previous studies involving diesel-like fuels [42, 43].

To aid with the interpretation of the schlieren images, the associated HRR profiles are also plotted and presented in Fig. 6. The HRR profiles rise at about 3.1 ms aSOI and 3.4 ms aSOI for the PRF100 and PRF0 cases, respectively. The timings at which the heat release rates begin to increase approximately coincide with the time instants when regions of dark contrast first appear in the schlieren images of the fuels. In both cases, the HRR profiles show the typical characteristics of an igniting jet. The profiles are characterised by rapid rises in HRRs, before transitioning towards more transient steady-state rates. Compared with the PRF100 case, the PRF0 case shows a higher HRR peak. The higher peak is consistent with the longer ignition delay and the more rapid darkening over a greater extent of the PRF0 jet, as seen in its schlieren images.

The averaged ignition delays for the fuels, which were derived from the in-chamber pressure traces using the procedures detailed in Section 2.3.5, are 3.3±0.4 ms aSOI and 4.9±0.9 ms aSOI for the PRF100 and PRF0 jets, respectively. As is previously noted, the charge temperatures were selected to ensure that there is sufficient distance between the natural lift-off distance of the flames and the nozzle for the flame transient responses to be monitored during the LI tests. With the longer lift-off distance, a greater level of fuel-air mixing before autoignition can occur. This may lead to overmixing occurring at the ignition location of the fuel jet [53, 57], which can increase the level of uncertainty in the ignition timings of the fuels. Extensive analysis of all of the schlieren videos (not shown here for brevity) reveals that natural lift-off distances prior to LI of the PRF100 and PRF0 flames occur at approximately 42.7±5.7 mm and 43.7±6.8 mm, respectively. The average and standard deviation values of the ignition delays and the lift-off distances before LI of the fuels are summarised in Table. 4. It is noted that the liquid lengths are estimated to be 5.1 mm and 8.6 mm for PRF100 and PRF0 fuel jets, respectively. Despite the difference in the charge temperature and, hence, the vaporisation rates of the fuels, previous studies (*e.g.*, [58]) have suggested that the vaporisation sprays from direct-injection diesel fuel injectors are mixing-limited. The mixing-limited vaporisation assumption implies that the fuel-air mixing rates of the fuel sprays will not increase with more rapid fuel vaporisation. The ignition delay, the lift-off length, and the liquid length information of the natural autoignition cases, when taken together with the mixture distribution information in Section 3.1, show that the proposed LI locations and timings address the listed considerations in Section 2.2.1.

3.3. Forced laser ignition cases

Figures 7 and 8 present the schlieren image sequences that demonstrate the transient lift-offs of the laser-ignited PRF100 and PRF0 fuel jets, respectively. The image sequences were acquired at the same ambient conditions as the natural autoignition cases in Fig. 5. The timings for the schlieren images are indicated on the top-left corners of the image panels in the first left columns of Figs. 7 and 8. The yellow dashed lines in the figures indicate the minimum lift-off distances of the flames, when present, at different time instants. The red crosses give the LI locations for the test cases.

Figures 7 (first and second columns) show that the darkened schlieren contrast regions tend to stabilise at 40–50 mm shortly after their first appearances. For the PRF100/15/5.28 case (Fig. 7, first column), an 'isolated' darkened region spontaneously forms at 45 mm from the nozzle, upstream of the main flame body, at 4.09 ms aSOI. From 4.09 to 5.29 ms aSOI, the size of the detached darkened region appears to grow and merge with the main flame body. The merging event leads to a rapid decrease in the lift-off distance of the whole lifted flame to approximately 45 mm from the nozzle, where the isolated darkened region first appears. At 5.28 ms aSOI, which is after the natural autoignition timing of 3.3 ms aSOI for the PRD100 flame at 900 K condition, focused laser beams were fired at 15 mm and 30 mm from the nozzle for the PRF100/15/5.28 and PRF100/30/5.28 cases, respectively. The laser perturbations lead to the forming of isolated darkened regions at the LI locations. The isolated darkened regions then proceed to grow in their sizes before merging with the other darkened regions of the downstream flame bodies. At the time instants when the formation and the merging events occur, the calculated lift-off distances reduce to the LI locations but gradually shift downstream over time. The lift-off distances of the downstream lifted flames appear largely unaffected by the upstream events, as they change little in terms of their axial positions before the merging events.

Figure 7 (third and fourth columns) show the schlieren image sequences for the PRF100/15/2.28 and PRF100/30/2.28 cases. At 2.28 ms aSOI, which is before the natural ignition delay timing for the PRF100 flame at 900 K condition, focused laser beams were fired at 15 mm and 30 mm from the nozzle for the PRF100/15/2.28 and PRF100/30/2.28 cases, respectively. At the same time instant, the tips of the non-reactive jets have reached 45 mm from the nozzle, as seen from the schlieren images. The LI events lead to the forming of isolated darkened regions at the LI locations. The darkened regions then appear to increase in size and grow in connected reaction regions until they match the boundaries of the non-reactive jets. As the darkened regions quickly propagate downstream, the calculated lift-off distances for both cases remain close to the LI position. The laser-affected lift-off locations of the flames, however, proceed to slowly shift downstream with time.

Comparing the schlieren image sequences for the PRF100 fuel in Fig. 7 and 5, the downstream regions of the schlieren images show increased luminosity after the LI events, for the PRF100/15/5.28 and PRF100/15/2.28 cases

with LI locations at 15 mm from the nozzle. When compared with the schlieren images from the earlier time instants, the schlieren signal of the PRF100/15/5.28 case noticeably brightens from 35 mm and towards the jet head, from 6.29 to 7.29 ms aSOI. For the PRF100/15/2.28 case, the schlieren signal also brightens considerably towards the jet head region, as seen in the schlieren images in the regions downstream of 15 mm from the nozzle, from 2.79 to 3.55 ms aSOI. The observed change in the image intensity, albeit over a comparatively short duration relative to the entire injection duration, indicates a potential increase in the soot levels of the flame jets. No observable increase in the luminosity level, however, are observed in the schlieren image sequences of the natural autoignition and the forced LI cases with more downstream LI locations. Together, the observations imply that the fuel-air mixing levels at regions that are upstream of the natural lift-off distance or the forced LI locations of 30 mm are sufficient to produce little or no soot. It is noted that previous soot studies have observed that the diesel fuel jet soot decreases with increasing fuel-air premixing upstream of the lift-off length, with the cross-sectional average equivalence ratio at the lift-off length ($\overline{\phi_H}$) demonstrated to provide a useful estimate of the latter [59]. Previous soot studies also reported observable soot luminosity when the $\overline{\phi_H}$ value exceeds 2 [59]. For this study, rough estimates of the equivalence ratio values at the different natural or laser-forced lift-off locations are derived from the 1D model results presented in Fig. 4. As is noted in Section 3.1, the model shows the $\overline{\phi_H}$ at 15 mm and 30 mm from the nozzle are 2.8 and 0.7, respectively. The observation of the increased luminosity within the fuel jet only at a laser-forced lift-off location of 15 mm (*i.e.*, $\overline{\phi_H}$ greater than a value of 2) appears consistent with the findings of previous studies.

Figure 8 shows the schlieren image sequences for the laser-ignited PRF0 fuel jets. For PRF100, two LI positions of 15 mm and 30 mm from the nozzle. are shown with two LI timings of 6.28 ms aSOI (*i.e.*, after the natural lift-off length was established) and 2.28 ms aSOI (*i.e.*, before the natural autoignition of the fuel jets). The PRF0 jets display trends that are similar to that of PRF100 flames. In brief, the LI events result in the forming of isolated regions with dark schlieren contrast, which then grow in connected regions to either merge with the downstream reacting jets (*cf.* Fig. 8, first and second columns) or to match the boundaries of the non-reacting jets (*cf.* Fig. 8, third and fourth columns) downstream. The darkened regions first stabilise at locations that are close to the LI locations before slowly increase in distance away from the nozzle with time, until the end of the injections. Compared with PRF100, however, there is no apparent brightening in the schlieren images of the PRF0 test cases with LI.

3.4. Effects of laser ignition location and timing on flame lift-off

Figure 9 shows the effect of the LI location and timing on the temporal evolution of the lift-off distances for the fuel jets, which are derived from the schlieren recordings of the different LI cases. The traces presented were ensemble-averaged from at least 10 experimental repetitions for each test case. The uncertainties (1 standard deviation) of the traces are presented as colour-shaded regions in the figure. In the figure, the test cases with two LI positions along

with two LI laser timings, which correspond to time instants before and after the natural flame lift-off lengths have been established, are shown.

Figure 9 (left) shows that in the PRF100 cases (*i.e.*, PRF100/15/5.28 and PRF100/30/5.28) where the fuel jets were allowed to naturally autoignite before the LI events, the flames display considerable positional uncertainties, with standard deviation values ranging from 5.44 mm to 6.21 mm, prior to the LI events. The figure also shows that the LI events at 5.28 ms aSOI alter the initial lift-off distances to locations that are close to the LI positions (*i.e.*, 15 mm and 30 mm from the nozzle). The standard deviations associated with the laser-forced lift-off locations at the LI timings appear to reduce to values ranging from 0.61 mm to 1.19 mm, which correspond to a reduction that is greater than 80% when compared to the natural occurring lift-offs. The positional uncertainties of the laser-affected lift-off lengths, nevertheless, increase in magnitude as the flames stabilisation positions approach their natural lift-off lengths. The standard deviations of the flame laser-affected lift-offs increase to values ranging from 2.10 mm to 2.78 mm at the end-of-injections (EOIs) but are still lower than that observed for the natural lift-offs before LI.

Figure 9 (left) also shows that for the cases where the laser beams were positioned (*i.e.*, 30 mm) closer to the natural lift-offs, the flames appear to shift away from the nozzle before transitioning into a more quasi-steady state, where the increase rates of the lift-off distances become less apparent. For the cases where the laser beams were focused at locations closer to the injectors (*i.e.*, 15 mm), the flames shift towards the directions of their natural lift-offs with time, after LI. The trends from the figure indicate that these flames do not appear to transition into a more quasi-steady state before their EOIs.

When analysing the cases where the fuel jets experienced laser-forced ignition before autoignition (*i.e.*, PRF100/15/2.28 and PRF100/30/2.28), it can be seen that the flames stabilise at the LI positions before shifting downstream towards the direction of their natural lift-off locations. The uncertainties of the flame lift-offs increase from values of 0.66—0.73 mm at the LI positions to 1.70—2.32 mm at the EOIs. Similar to the LI cases where the flames were allowed to establish quasi-steady lift-offs before laser perturbations (*i.e.*, PRF100/15/5.28 and PRF100/30/5.28), the PRF100 flame that was forced-ignited at 30 mm from the nozzle (*i.e.*, PRF100/30/2.28) appear to transition into a more quasi-steady state before its EOI. The same, however, is not observed for the PRF100 flame that was forced-ignited at a location that is closer to the nozzle (*i.e.*, PRF100/15/2.28). Despite the long injection duration used (*i.e.*, 11.5 ms), the figure shows that the flame does not revert to its natural lift-off distance before its EOI. It is noted that a previous study [43] performed a systematic investigation of the temporal evolutions of flame lift-offs, when diesel fuel jets were also laser-ignited in regions upstream of their natural occurring lift-off distances, at engine-relevant conditions in a constant-volume combustion chamber. The study proposed that the LI event that occurs at a location that is upstream of the natural flame lift-off location can produce a reservoir of high-temperature gases at the jet edge,

which consists of combustion products and entrained ambient gases. The previous study suggested that the turbulent macro-mixing and entrainment from the reservoir of hot gases can lower local strain and turbulence levels in the shear flows. Additionally, it was proposed that the interaction of the laser-induced reservoir of hot products at the jet peripheral with the incoming fuel-air mixture may assist the ignition of the fresh charge. All these factors may lead to the observed upstream flame stabilisation after LI. The study, however, also noted that the depletion of the reservoir of hot products over time can result in the shifting of the flame lift-off from the LI position towards its natural lift-off location. While not conclusive, the observations of this work do not appear to be inconsistent with the hypothesis of the previous study.

Figure 9 (right) shows that the lift-off distance trends of the PRF0 cases are similar to that of the PRF100 flames, but with some exceptions. Whereas the PRF0 flames also stabilise at the LI locations after the forced-ignition events, the time that the PRF0 flames take to return to their natural distances are comparatively shorter. The differences are more apparent for the cases where LI locations are closer to the nozzle. For example, using an axial distance of 25 mm from the nozzle as a reference point, Fig. 9 (left) shows that for the PRF100 jets, the forced-ignition events at 15 mm from the nozzle before and after natural ignition (*i.e.*, PRF100/15/5.28 and PRF100/15/2.28) stabilise the flame lift-offs at locations that are upstream to the reference position upstream for approximately 6 ms. Figure 9 (right), however, shows that for the PRF0 test cases that underwent force-ignitions at the same upstream location (*i.e.*, PRF0/15/6.28 and PRF0/15/2.28), the time that the flame bases take to shift from the LI locations to the reference point is comparatively shorter, at about 3 ms after LI. Considering the shorter upstream stabilisation periods that the PRF0 cases display, it is therefore also within the expectation that a majority of the investigated PRF0 cases (*i.e.*, PRF0/30/5.28, PRF0/30/2.28 and PRF0/150/2.28) start transitioning into a more quasi-steady state before their EOIs. Table 5 provides a summary of the uncertainties associated with the flame lift-off lengths for both fuels, at different time instants, including before LI, after LI and at the EOI.

The proposed theory of peripheral reservoir of hot products assisting flame stabilisation [43] also supports the observations of the longer upstream stabilisation period that the PRF100 flames display relative to the PRF0 cases. As is noted previously, for the purpose of this work, the PRF100 flames were subjected to a higher ambient temperature condition when compared with the PRF0 cases to account for the differences in the fuel reactivities. The hypothesised peripheral product reservoirs and the incoming fuel-air mixtures of the PRF100 cases are, therefore, also likely to have higher temperatures. Therefore, a possible reason for the longer period of upstream stabilisation is the more gradual depletion of the hot product reservoirs of the PRF100 cases, as a lesser amount of entrained hot products is required to ignite the incoming fuel-air charge of the PRF100 flames. It is, nonetheless, emphasised that this does not rule out other potential mechanisms.

3.5. Effects of laser ignition location and timing on heat release rate and total luminosity

A consequence of changing the flame lift-off stabilisation is the modification of the reacting fuel-air mixture involved, and subsequently, its HRR profile. It is noted that HRR measurements are widely used in previous diesel studies to detect high-temperature ignition, which is associated with significant heat release that occurs during the premixed-burn phase of the diesel combustion. A mixing-controlled combustion period typically follows, during which the heat release is approximately proportional to the fuel-air mixing rate [46, 60].

Figure 10 (left) presents the HRR profiles corresponding to the LI events of the PRF100 flames. The colour-shaded areas in the figure represent the corresponding uncertainties of the profiles. For the cases where laser perturbations occurred after the natural autoignition of the fuel jets (*i.e.*, PRF100/15/5.28 and PRF100/30/5.28), the HRR profiles of the jets peak after the natural autoignition and forced ignition events. In both instances, the HRR rates level off to lower steady values after the peaks, which suggest their transitions into mixing-controlled combustion. For the cases where the fuel jets experienced laser perturbations prior to their natural autoignition events (*i.e.*, PRF100/15/2.28 and PRF100/30/2.28), the HRR profiles only show a single distinguishable burn peak, which is followed by lower steady HRR after.

In terms of LI location variation, Fig. 10 (left) shows at the same LI timing, the peak HRR value is comparatively higher for the test cases with LI locations that are closer to the injection nozzle (*i.e.*, PRF100/15/2.28 and PRF100/15/5.28), when compared to the cases with LI locations that are further downstream (*i.e.*, PRF100/30/2.28 and PRF100/30/5.28). This is to be expected considering that at ignition, the peak HRR value depends on the distribution as well as the mass of the readily ignitable fuel-air mixture within the jet [60]. In terms of LI timing variation, the figure shows that at the same LI location, the peak HRR value is comparatively higher for cases where laser perturbations occurred after the natural autoignition events (*i.e.*, PRF100/15/5.28 and PRF100/30/5.28), when compared to the cases with LI events that took place before the natural autoignition of the flames (*i.e.*, PRF100/15/2.28 and PRF100/30/2.28). This is to be expected, considering that the peak HRR value of the former comprises of the heat release arising from the laser-ignited mixtures, in addition to the heat release from the established diffusion flames.

Figure 10 (right) presents the HRR profiles corresponding to the LI events of the PRF0 flames. The HRR trends of the PRF0 are, in general, similar to the PRF100 cases, albeit with some differences. For the PRF0 cases where the fuel jets were allowed to transition into quasi-steady states before laser perturbations (*i.e.*, PRF0/15/6.28 and PRF0/30/6.28), the average HRR profiles appear to quickly increase to level off at near quasi-steady values. A close inspection of the uncertainties of the average HRR profiles and the actual individual profiles (not shown for brevity), however, indicates the presence of significant run-to-run variations. This is expected as the PRF0 flames were subjected to low ambient temperature conditions. A majority of the individual profiles still displays a pro-

nounced premixed-burn peak that is followed by a lower heat release period after—features that are not captured by the average profiles alone. The variability in the timing and the magnitude of the heat release processes, which are associated with the natural ignition events, therefore, may affect the LI events after. This can contribute to the greater variability in the magnitudes of the peak HRR values after the LI events of the PRF0 flames when compared to that observed for the PRF100 cases.

The changing of the flame lift-off stabilisation with LI is also expected to affect the soot formation processes within the fuel jets [43, 50]. As is stated in Section 2.3.4, a photodiode was used to record the total luminosity from the fuel sprays from the front window of the combustion vessel. The measurement readings from the different test cases are presented in Fig. 11, and the values presented are normalised to the differences in gain settings used during experiments. In the figure, the intense emissions from the LI events appear in the forms of impulses at their respective timings (*i.e.*, 2.28, 5.28 and 6.28 ms aSOI). It is noted that the photodiode readings that were acquired for the injections without LI (not shown in the figure) show that fuel jets exhibit low luminosity, such that maximum readings of 0.0032 and 0.0028 V (after normalised by their photodiode gain settings) were measured for the PRF100 and PRF0 natural ignition cases, respectively. The results indicate that under the test conditions of this work, the fuel-air mixing levels at locations that are upstream to the natural lift-offs of the flames are sufficient to lead to little or no soot formation.

Figure 11 shows that the luminosity levels increase after the LI events, before declining back to values that are considerably lower than their local peaks, but still higher than the original luminosity levels before the laser perturbations. The increase in the luminosity level following LI events is consistent with the expected effect associated with the changing of the flame lift-off stabilisation position. The reacting fuel-air mixtures at the laser-induced lift-off locations that are closer to the nozzle (*i.e.*, 15 mm from the nozzle) can be expected to be more fuel-rich, which can lead to an increase in soot formation. Nonetheless, the lift-off lengths of the flames, however, increase in distance from the nozzle with time. The associated reacting fuel-air mixtures naturally become increasingly fuel-lean, which leads to less soot formation, and hence, a decrease in the total luminosity of the flame over time.

When analysing the PRF100 flames with LI events occurring at 15 mm from the nozzle, Fig. 11 (left) shows that the peak luminosity level for the case with an earlier LI timing of 2.28 ms aSOI (*i.e.*, PRF100/15/2.28) is higher than that with a later LI timing of 5.28 ms aSOI (*i.e.*, PRF100/15/5.28). It is known that the soot luminosity is dependent on the distribution and magnitude of the flame temperature and soot content within [61]. Therefore, while one expects the greater heat release of the PRF100/15/5.28 case (*c.f.* Fig. 10) can enhance the flame temperature, an increase in temperature can, nevertheless, also lead to an increase in soot formation [59]. Therefore, when the magnitudes of the total luminosity levels are comparable, more detailed measurements are required to ascertain the underlying factor.

Figure 11 (right) shows that the overall trends of the PRF0 cases are similar to the PRF100 cases, but with much

lower peak luminosity levels. The luminosity values of the PRF0 LI cases, whilst higher than the readings detected for their natural autoignition cases, are nevertheless still considerably lower than that of the PRF100 flames. Figure 12 demonstrates a possible reason for the higher luminosity levels of the PRF100/15/5.28 and PRF100/15/2.28 cases when compared to PRF0/15/6.28 and PRF100/15/2.28 cases. The figure is a plot of ϕ against the adiabatic mixture flame temperature, with a region of 'soot formation likely' highlighted. The adiabatic temperature was calculated by a zero-dimensional model of a constant-pressure homogeneous reactor [62]. A PRF skeletal mechanism with 121 species and 538 reactions was used [63] for the simulation and the fuel heat of vaporisation was accounted for. The *phi* (*i.e.*, ϕ¿2) and temperature (*i.e.*, 1600¡T¡2500) limits of the 'soot formation likely' region are derived from previous studies [64, 65]. The figure shows that adiabatic mixing and the reaction of the PRF100 flame pass through the 'soot formation likely' region in the 'ϕ-T' plot, whereas those associated with the PRF0 flame completely avoid the region. Consequently, although the estimated $\overline{\phi_H}$ values are 2.8 at 15 mm from the nozzle for both fuels (see Section 3.3), the lower charge temperature that was used for the PRF0 flame is sufficient to avoid the formation of soot. It is, nonetheless, important to note that a higher soot level within the reacting section of the fuel jet does not necessarily imply that a greater soot amount would emit from the flame. For example, previous soot studies (*e.g.*, [59]) of fuel jets at diesel conditions reported that while the peak soot levels of the jets increase with higher ambient temperature conditions, the associated soot oxidation processes are also enhanced. There are also previous post-injection studies that have attributed the observed reduction in engine-out particulate matter emissions in their studies to the elevated in-cylinder temperature conditions, arising from the additional heat release from the post-injection that was introduced [66, 67].

3.6. Conclusion

This work focused on improving the fundamental understanding of laser ignition (LI) effect on the ignition and combustion characteristics of gasoline-like fuel. In this work, a high-energy focused laser beam was used to generate a plasma at specific spatial locations and times after the start of injection (aSOI). High-speed schlieren imaging was used to monitor the transient ignition and combustion characteristics of the fuel jets in the presence and absence of laser spark induced ignition, under GCI engine relevant conditions. Primary reference fuel (PRF) *iso*-octane (*i.e.*, PRF100) was used as a gasoline surrogate to emulate the ignition characteristic of gasoline-like fuels, while a diesel surrogate *n*-heptane (*i.e.*, PRF0) was tested at similar laser ignition locations and timings for comparison purposes. Different charge temperatures were used to keep the lift-off lengths of the fuel jets approximately the same within a comparison set. This allowed the evaluation of the effects of LI events on the ignition and combustion processes of the different fuels, whilst keeping similar fuel-air mixture distribution conditions at the LI locations. A systematic analysis of fuel/air mixing, ignition characteristics, heat release and luminosity level, highlights the effect of LI on

PRF100 flame and its differences compared to PRF0 flame. Measurements of non-reacting jet penetration show similar jet behaviours for the PRFs, which supports the assumption of comparable mixture distributions upstream of flame lift-off lengths for both fuel jets.

Under the test conditions of this work, the natural autoignition cases of the fuels displayed slightly different ignition and flame stabilisation characteristics. For the PRF100 flame, isolated kernels that appeared upstream and detached from the main flame body were observed, after the initial autoignition events that occurred in the near jet head regions. The subsequent merging of the kernels with the main flame body was found to reduce the flame lift-off length. In the case of the PRF0 flame, however, no apparent ignition kernels were observed. The autoignition of the PRF0 flame was also found to occur more uniformly across a larger portion of the jet.

The transient flame structures of the LI cases were visualised using high-speed schlieren imaging. The temporal plots of the flame lift-off length, as derived from the schlieren images, showed that the uncertainties of flame lift-off lengths reduced after LI compared to those during the natural stabilisation periods. The plots also revealed that the laser-affected flame lift-off distances shifted towards the directions of their natural lift-offs after the LI events. For this work, the transient responses that flames displayed after laser perturbations appear to be explained by a previously hypothesised mechanism that is based on the turbulent mixing with high-temperature combustion produced formed at the jet peripherals.

The heat release rate (HRR) profiles of the flames were derived from the pressure measurements, which were also recorded during the experiments. When combining the HRR profiles with the observations from the schlieren recordings, the results indicate that LI ignition can ignite the previously unreacted fuel-air mixtures at the LI locations. The ignition events were found to lead to higher heat release rates, immediately after the LI events, before transitioning into lower steady values with increasing time. The magnitudes of the peak heat release rates appeared to be correlated to the LI positions/location mixture conditions.

The total flame luminosity levels were also measured using a photodiode during the experiments. The natural luminosity levels of the flames were observed to be low. The LI events, however, were observed to lead to an increase in the total luminosity levels of the flames. For the PRF100 flames, a more significant increase in the flame luminosity levels was observed when the PRF100 jets were forced ignited at a near-nozzle location. For the PRF0 cases, the changes in the luminosity levels, however, were found to be smaller. An analysis of the local mixture conditions using the simulation results from a one-dimensional jet model and a zero-dimensional model of a constant-pressure homogeneous reactor suggested that the local cross-sectional equivalence ratios of both flames of the laser-affected flame lift-offs, when they were positioned close to the nozzle, can become sufficiently fuel-rich to support soot formation. The soot levels within of the flames, nonetheless, were also affected by the different ambient temperature conditions

that the flames were subjected to.

References

[1] A. K. Agarwal, A. P. Singh, R. K. Maurya, Evolution, challenges and path forward for low temperature combustion engines, Progress in Energy and Combustion Science 61 (2017) 1–56.

[2] M. P. Musculus, P. C. Miles, L. M. Pickett, Conceptual models for partially premixed low-temperature diesel combustion, Progress in Energy and Combustion Science 39 (2-3) (2013) 246–283.

[3] R. D. Reitz, Directions in internal combustion engine research, Combustion and Flame 160 (1) (2013) 1–8.

[4] G. Kalghatgi, B. Johansson, Gasoline compression ignition approach to efficient, clean and affordable future engines, Proceedings of the Institution of Mechanical Engineers, Part D: Journal of Automobile Engineering 232 (1) (2018) 118–138.

[5] K. Cung, A. Moiz, M. Smith, C. Bitsis, T. Briggs, J. Miwa, Gasoline compression ignition GCI combustion of pump-grade gasoline fuel under high compression ratio diesel engine, Transportation Engineering (2021) 100066.

[6] G. T. Kalghatgi, P. Risberg, H.-E. Ångström, Advantages of fuels with high resistance to auto-ignition in late-injection, low-temperature, compression ignition combustion, SAE Paper (2006) 2006–01–3385.

[7] G. T. Kalghatgi, P. Risberg, H.-E. Ångström, Partially pre-mixed auto-ignition of gasoline to attain low smoke and low NO_x at high load in a compression ignition engine and comparison with a diesel fuel, SAE Paper (2007) 2007–01–0006.

[8] G. Kalghatgi, L. Hildingsson, B. Johansson, Low NO_x and low smoke operation of a diesel engine using gasoline like fuels, Journal of Engineering for Gas Turbines and Power 132 (9) (2010).

[9] A. César, J. Carvalho Jr, L. Nascimento, Association between NO_x exposure and deaths caused by respiratory diseases in a medium-sized brazilian city, Brazilian Journal of Medical and Biological Research 48 (12) (2015) 1130–1135.

[10] C. A. Pope III, D. W. Dockery, J. D. Spengler, M. E. Raizenne, Respiratory health and pm10 pollution: a daily time series analysis, American Review of Respiratory Disease 144 (3_pt_1) (1991) 668–674.

[11] Z. D. Ristovski, B. Miljevic, N. C. Surawski, L. Morawska, K. M. Fong, F. Goh, I. A. Yang, Respiratory health effects of diesel particulate matter, Respirology 17 (2) (2012) 201–212.

[12] G. Kalghatgi, L. Hildingsson, A. Harrison, B. Johansson, Autoignition quality of gasoline fuels in partially premixed combustion in diesel engines, Proceedings of the Combustion Institute 33 (2) (2011) 3015–3021.

[13] L. Hildingsson, G. Kalghatgi, N. Tait, B. Johansson, A. Harrison, Fuel octane effects in the partially premixed combustion regime in compression ignition engines, SAE Paper (2009) 2009–01–2648.

[14] V. Manente, C.-G. Zander, B. Johansson, P. Tunestal, W. Cannella, An advanced internal combustion engine concept for low emissions and high efficiency from idle to max load using gasoline partially premixed combustion, SAE Paper (2010) 2010–01–2198.

[15] V. Manente, B. Johansson, W. Cannella, Gasoline partially premixed combustion, the future of internal combustion engines?, International Journal of Engine Research 12 (3) (2011) 194–208.

[16] C. P. Kolodziej, S. Ciatti, D. Vuilleumier, B. D. Adhikary, R. D. Reitz, Extension of the lower load limit of gasoline compression ignition with 87 AKI gasoline by injection timing and pressure, SAE Paper (2014) 2014–01–1302.

[17] C. Kolodziej, J. Kodavasal, S. Ciatti, S. Som, N. Shidore, J. Delhom, Achieving stable engine operation of gasoline compression ignition using 87 AKI gasoline down to idle, SAE Paper (2015) 2015–01–0832.

[18] P. Borgqvist, P. Tunestal, B. Johansson, Comparison of negative valve overlap (NVO) and rebreathing valve strategies on a gasoline PPC engine at low load and idle operating conditions, SAE International Journal of Engines 6 (1) (2013) 366–378.

[19] M. Sellnau, M. Foster, W. Moore, J. Sinnamon, K. Hoyer, W. Klemm, Pathway to 50% brake thermal efficiency using gasoline direct injection compression ignition, SAE International Journal of Advances and Current Practices in Mobility 1 (2019-01-1154) (2019) 1581–1603.

[20] M. Weinrotter, E. Wintner, K. Iskra, T. Neger, J. Olofsson, H. Seyfried, M. Aldén, M. Lackner, F. Winter, A. Vressner, et al., Optical diagnostics of laser-induced and spark plug-assisted hcci combustion, SAE Paper (2005) 2005–01–0129.

[21] J. Benajes, A. García, V. Domenech, R. Durrett, An investigation of partially premixed compression ignition combustion using gasoline and spark assistance, Applied Thermal Engineering 52 (2) (2013) 468–477.

[22] R. F. Cracknell, J. Ariztegui, T. Dubois, H. Hamje, L. Pellegrini, D. Rickeard, K. D. Rose, K. Deppenkemper, B. Graziano, K. A. Heufer, et al., Modelling a gasoline compression ignition (gci) engine concept, SAE Paper (2014) 2014–01–1305.

[23] H. Yun, C. Idicheria, P. Najt, The effect of advanced ignition system on gasoline low temperature combustion, International Journal of Engine Research 22 (2) (2021) 417–429.

[24] E. Nakai, T. Goto, K. Ezumi, Y. Tsumura, K. Endou, Y. Kanda, T. Urushihara, M. Sueoka, M. Hitomi, Mazda skyactiv-x 2.0 l gasoline engine, in: Proceedings of the 28th Aachen colloquium automobile and engine technology, Vol. 2019, 2019, pp. 1–28.

[25] M. H. Morsy, Review and recent developments of laser ignition for internal combustion engines applications, Renewable and Sustainable Energy Reviews 16 (7) (2012) 4849–4875.

[26] N. Pavel, M. Bärwinkel, P. Heinz, D. Brüggemann, G. Dearden, G. Croitoru, O. V. Grigore, Laser ignition-spark plug development and application in reciprocating engines, Progress in Quantum Electronics 58 (2018) 1–32.

[27] J. V. Pastor, J. M. García-Oliver, A. García, M. Pinotti, Effect of laser induced plasma ignition timing and location on diesel spray combustion, Energy Conversion and Management 133 (2017) 41–55.

[28] M. Weinrotter, H. Kopecek, E. Wintner, M. Lackner, F. Winter, Application of laser ignition to hydrogen–air mixtures at high pressures, International journal of hydrogen energy 30 (3) (2005) 319–326.

[29] F. J. Weinberg, J. R. Wilson, A. G. Gaydon, A preliminary investigation of the use of focused laser beams for minimum ignition energy studies, Proceedings of the Royal Society of London. A. Mathematical and Physical Sciences 321 (1544) (1971) 41–52. doi:10.1098/rspa.1971.0012.

[30] T. X. Phuoc, F. P. White, Laser-induced spark ignition of CH4/air mixtures, Combustion and flame 119 (3) (1999) 203–216.

[31] J. Tauer, H. Kofler, E. Wintner, Laser-initiated ignition, Laser & Photonics Reviews 4 (1) (2010) 99–122.

[32] T. Alger, D. Mehta, C. Chadwell, C. Roberts, Laser ignition in a pre-mixed engine: The effect of focal volume and energy density on stability and the lean operating limit, SAE Paper (2005) 2005–01–3752.

[33] H. Kopecek, E. Wintner, M. Lackner, F. Winter, A. Hultqvist, Laser-stimulated ignition in a homogeneous charge compression ignition engine, SAE Paper (2004) 2004–01–0937.

[34] J. Mullett, R. Dodd, C. Williams, G. Triantos, G. Dearden, A. Shenton, K. Watkins, S. Carroll, A. Scarisbrick, S. Keen, The influence of beam energy, mode and focal length on the control of laser ignition in an internal combustion engine, Journal of Physics D: Applied Physics 40 (15) (2007) 4730.

[35] C. Xu, D. Fang, Q. Luo, J. Ma, Y. Xie, A comparative study of laser ignition and spark ignition with gasoline–air mixtures, Optics & Laser Technology 64 (2014) 343–351.

[36] J. V. Pastor, J. M. García-Oliver, A. García, C. Micó, Combustion improvement and pollutants reduction with diesel-gasoline blends by means of a highly tunable laser plasma induced ignition system, Journal of Cleaner Production 271 (2020) 122499.

[37] Q. Chan, I. R. Fattah, G. Zhai, H. Yip, T. Chen, A. Yuen, W. Yang, A. Wehrfritz, X. Dong, S. Kook, et al., Color-ratio pyrometry methods for flame–wall impingement study, Journal of the Energy Institute 92 (6) (2019) 1968–1976.

[38] T.-C. Chi, G. Zhai, S. Kook, Q. Chan, E. R. Hawkes, Application of LED-based thermographic phosphorescent technique to diesel combustion chamber walls in a pre-burn-type optical constant-volume vessel, Experiments in Fluids 60 (2) (2019) 34.

[39] I. M. R. Fattah, C. Ming, Q. N. Chan, A. Wehrfritz, P. X. Pham, W. Yang, S. Kook, P. R. Medwell, G. H. Yeoh, E. R. Hawkes, A. R. Masri, Spray and combustion investigation of post injections under low-temperature combustion conditions with biodiesel, Energy & Fuels 32 (8) (2018) 8727–8742.

[40] N. Atef, J. Badra, M. Jaasim, H. G. Im, S. M. Sarathy, Numerical investigation of injector geometry effects on fuel stratification in a GCI engine, Fuel 214 (2018) 580–589.

[41] M. L. Wissink, S. J. Curran, G. Roberts, M. P. Musculus, C. Mounaïm-Rousselle, Isolating the effects of reactivity stratification in reactivity-controlled compression ignition with iso-octane and n-heptane on a light-duty multi-cylinder engine, International Journal of Engine Research 19 (9) (2018) 907–926.

[42] F. Tagliante, L.-M. Malbec, G. Bruneaux, L. M. Pickett, C. Angelberger, Experimental study of the stabilization mechanism of a lifted diesel-type flame using combined optical diagnostics and laser-induced plasma ignition, Combustion and Flame 197 (2018) 215–226.

[43] L. M. Pickett, S. Kook, H. Persson, Ö. Andersson, Diesel fuel jet lift-off stabilization in the presence of laser-induced plasma ignition, Proceedings of the Combustion Institute 32 (2) (2009) 2793–2800.

[44] N. Otsu, A threshold selection method from gray-level histograms, IEEE transactions on systems, man, and cybernetics 9 (1) (1979) 62–66.

[45] J. V. Pastor, R. Payri, J. M. Garcia-Oliver, J.-G. Nerva, Schlieren measurements of the ECN-spray A penetration under inert and reacting conditions, SAE Paper (2012) 2012–01–0456.

[46] B. Higgins, D. Siebers, A. Aradi, Diesel-spray ignition and premixed-burn behavior, SAE Paper (2000) 2000–961–984.

[47] P. M. Lillo, L. M. Pickett, H. Persson, O. Andersson, S. Kook, Diesel spray ignition detection and spatial/temporal correction, SAE International Journal of Engines 5 (3) (2012) 1330–1346.

[48] M. F. Brunt, H. Rai, A. L. Emtage, The calculation of heat release energy from engine cylinder pressure data, SAE transactions (1998) 1596–1609.

[49] J. V. Pastor, J. J. López, J. M. García, J. M. Pastor, A 1d model for the description of mixing-controlled inert diesel sprays, Fuel 87 (13-14) (2008) 2871–2885.

[50] L. M. Pickett, D. L. Siebers, C. A. Idicheria, Relationship between ignition processes and the lift-off length of diesel fuel jets, SAE Paper (2005) 2005–01–3843.

[51] J. D. Naber, D. L. Siebers, Effects of gas density and vaporization on penetration and dispersion of diesel sprays, SAE Paper (1996) 1996–82–111.

[52] L. M. Pickett, J. Manin, C. L. Genzale, D. L. Siebers, M. P. Musculus, C. A. Idicheria, Relationship between diesel fuel spray vapor penetration/dispersion and local fuel mixture fraction, SAE International Journal of Engines 4 (1) (2011) 764–799.

[53] G. Zhai, S. Xing, A. Yuen, G. Yeoh, Q. Chan, Spray and combustion characteristics of gasoline-like fuel under compression-ignition conditions, Energy & Fuels 34 (12) (2020) 16585–16598.

[54] S. Xing, G. Zhai, H. Mo, P. R. Medwell, A. C. Yuen, S. Kook, G. H. Yeoh, Q. N. Chan, Study of ignition and combustion characteristics of consecutive injections with iso-octane and n-heptane as fuels, Energy & Fuels 34 (11) (2020) 14741–14756.

[55] S. A. Skeen, J. Manin, L. M. Pickett, Simultaneous formaldehyde PLIF and high-speed schlieren imaging for ignition visualization in high-pressure spray flames, Proceedings of the Combustion Institute 35 (3) (2015) 3167–3174.

[56] S. Skeen, J. Manin, L. M. Pickett, Visualization of ignition processes in high-pressure sprays with multiple injections of n-dodecane, SAE International Journal of Engines 8 (2) (2015) 696–715.

[57] G. Lequien, S. Skeen, J. Manin, L. Pickett, O. Andersson, Ignition quality effects on lift-off stabilization of synthetic fuels, SAE International Journal of Engines 8 (2015).

[58] D. L. Siebers, Scaling liquid-phase fuel penetration in diesel sprays based on mixing-limited vaporization, SAE Paper (1999) 1999–01–0528.

[59] L. M. Pickett, D. L. Siebers, Soot in diesel fuel jets: effects of ambient temperature, ambient density, and injection pressure, Combustion and Flame 138 (2004) 114–135.

[60] H. L. Yip, A. Srna, X. Liu, S. Kook, E. R. Hawkes, Q. N. Chan, Visualization of hydrogen jet evolution and combustion under simulated direct-injection compression-ignition engine conditions, International Journal of Hydrogen Energy (2020).

[61] I. M. R. Fattah, H. L. Yip, Z. Jiang, A. C. Yuen, W. Yang, P. R. Medwell, S. Kook, G. H. Yeoh, Q. N. Chan, Effects of flame-plane wall impingement on diesel combustion and soot processes, Fuel 255 (2019) 115726.

[62] D. G. Goodwin, R. L. Speth, H. K. Moffat, B. W. Weber, Cantera: An object-oriented software toolkit for chemical kinetics, thermodynamics, and transport processes, `https://www.cantera.org`, version 2.5.1 (2021). doi:10.5281/zenodo.4527812.

[63] P. Pal, Y. Wu, T. Lu, S. Som, Y. C. See, A. Le Moine, Multi-dimensional CFD simulations of knocking combustion in a CFR engine, in: Internal Combustion Engine Division Fall Technical Conference, Vol. 58325, American Society of Mechanical Engineers, 2017, p. V002T06A017.

[64] K. Akihama, Y. Takatori, K. Inagaki, S. Sasaki, A. M. Dean, Mechanism of the smokeless rich diesel combustion by reducing temperature, Sae Paper (2001) 2001–01–0655.

[65] L. M. Pickett, D. L. Siebers, Non-sooting, low flame temperature mixing-controlled di diesel combustion, SAE Paper (2004) 2004–01–1399.

[66] M. Bobba, M. Musculus, W. Neel, Effect of post injections on in-cylinder and exhaust soot for low-temperature combustion in a heavy-duty diesel engine, SAE International Journal of Engines 3 (2010) 496–516.

[67] E. Mancaruso, S. S. Merola, B. M. Vaglieco, Study of the multi-injection combustion process in a transparent direct injection common rail diesel engine by means of optical techniques, International Journal of Engine Research 9 (2008) 483–498.

Experimental conditions	
Nozzle diameter [μm]	105 (single-hole)
Ambient O_2 concentration [vol.%]	21 (reacting), 0 (non-reacting)
Ambient gas density [kg/m^3]	22.8
Ambient gas pressure [MPa]	5.2, 4.0
Ambient gas temperature [K]	900, 735
Injection pressure [MPa]	70
Injection duration [ms]	11.5

Table 1: Summary of the experimental conditions.

Property	**Fuel**	
	Iso-octane (PRF100)	*n*-Heptane (PRF0)
Formula	C_8H_{18}	C_7H_{16}
Stoichiometric mixture fraction	0.06237	0.06218
Boiling point [°C]	99.2	98.4
Density [kg/m^3] (20 °C)	691.9	683.7

Table 2: Fuel properties for *iso*-octane (PRF100) and *n*-heptane (PRF0). Stoichiometric mixture fractions were calculated at 21 vol.% ambient O_2 level.

Case	Fuel	Laser ignition (LI) location [mm]	LI time aSOI [ms]	Label
1	PRF100	15	5.28	PRF100/15/5.28
2	PRF100	30	5.28	PRF100/30/5.28
3	PRF100	15	2.28	PRF100/15/2.28
4	PRF100	30	2.28	PRF100/30/2.28
5	PRF0	15	6.28	PRF0/15/6.28
6	PRF0	30	6.28	PRF0/30/6.28
7	PRF0	15	2.28	PRF0/15/2.28
8	PRF0	30	2.28	PRF0/30/2.28

Table 3: Summary of test parameters.

Value	**Fuel**	
	PRF100	PRF0
Ignition delay [ms aSOI]	3.3±0.4	4.9±0.7
Lift-off length prior to LI (PRF100/5.28 ms aSOI, PRF0/6.28 ms aSOI) [mm]	42.7±5.7	43.7±6.8

Table 4: Summary of the average and standard deviation values for the natural ignition delays and lift-off lengths of the PRF100 and PRF0 flames.

Case	Before LI [mm]	After LI [mm]	At EOI [mm]
PRF100/15/5.28	6.21	1.19	2.10
PRF100/30/5.28	5.44	0.61	2.78
PRF100/15/2.28	-	0.73	1.70
PRF100/30/2.28	-	0.66	2.32
PRF0/15/6.28	5.43	0.65	0.98
PRF0/30/6.28	7.87	0.96	2.62
PRF0/15/2.28	-	1.05	3.27
PRF0/30/2.28	-	1.27	2.36

Table 5: Summary of the uncertainties of flame lift-off lengths at different time instants, including before laser ignition (LI), after LI and at the end-of-injection (EOI).

List of Figures

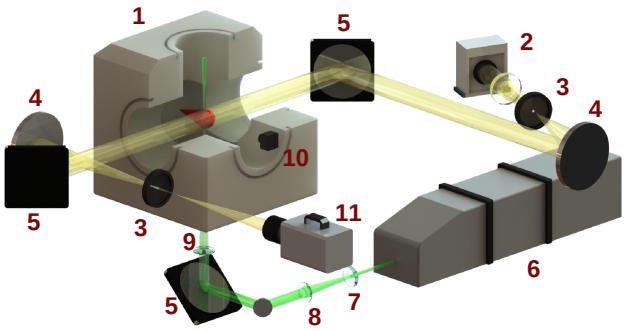

Figure 1: Schematic diagram of the constant-volume combustion chamber (CVCC) and setups used for high-speed schlieren imaging with laser-induced plasma ignition. Yellow regions indicate optical path for schlieren imaging. Green regions indicate laser path. Red region indicates flame jet. Components: 1. CVCC (section view); 2. Xenon arc lamp; 3. Iris; 4. Parabolic mirror; 5. Reflector; 6. Nd:YAG laser; 7. Convex lens (25 mm Dia. $\times$ 300 mm FL); 8. Concave lens (25 mm Dia. $\times -100$ mm FL); 9. Convex lens (25 mm Dia. $\times$ 150 mm FL); 10. Photodiode; 11. CMOS camera.

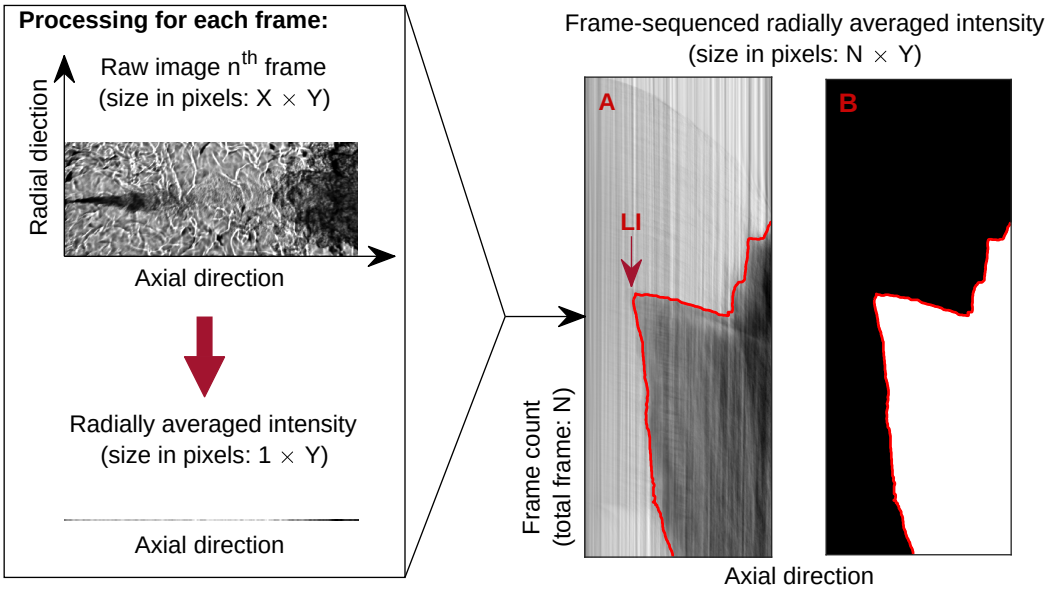

Figure 2: A schematic demonstration of the image processing procedure used to derive flame lift-off length information from a time-sequenced schlieren recording of a PRF100 flame (PRF100/15/5.28, Case 1). A sample of the schlieren image acquired at 5.32 ms aSOI is presented. Radial averaging was first performed for each frame of an *N*-frames time-sequenced schlieren series to produce *N* single-row vectors. The concatenation of the single-row vectors produced a frame-sequenced matrix (Matrix 'A'). A thresholding technique was then applied to generate a binarised matrix (Matrix 'B'). The temporal evolution of the flame lift-off information was then derived from the edge (shown as a red solid line) of the binarised region of Matrix 'B'. The red arrow in Matrix 'A', indicates the pixel that corresponds to the time instant at which laser ignition was introduced for the test case.

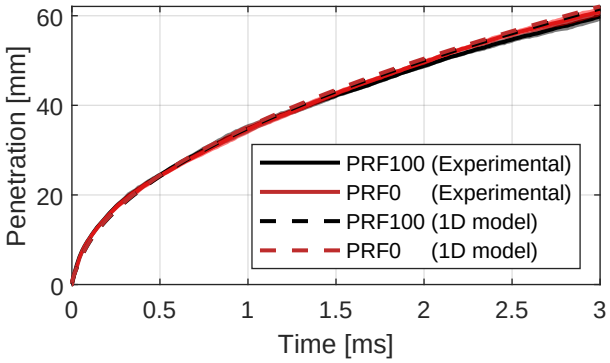

Figure 3: Plots of experimental penetration derived from schlieren images for PRF100 and PRF0, overlapping with the penetrations from one-dimensional jet simulations for PRF100 and PRF0. Colour-shaded areas represent standard deviations of the experimental data trends. For interpretations of the references to colour in this figure, the reader is referred to the web version of this article.

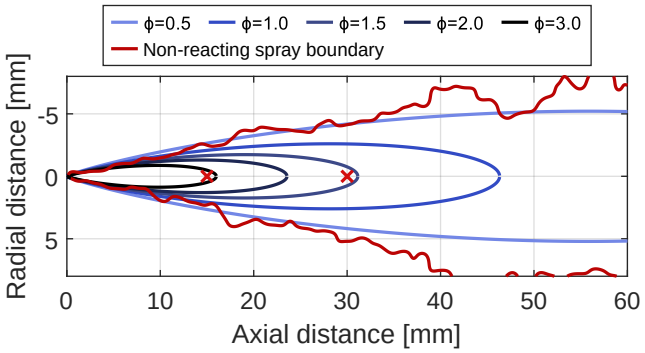

Figure 4: Equivalence ratio distributions estimated from one-dimensional jet simulation for PRF100. Ambient conditions: 900 K. Red crosses on the figure indicate the laser ignition locations (*i.e.*, at 15 mm and 30 mm along the jet centre-line from the injector nozzle). Red solid lines represent the non-reacting jet boundary extracted from a schlieren image of PRF100 at 6.28 ms aSOI, when the jet can be expected to be in a quasi-steady state. For interpretations of the references to colour in this figure, the reader is referred to the web version of this article.

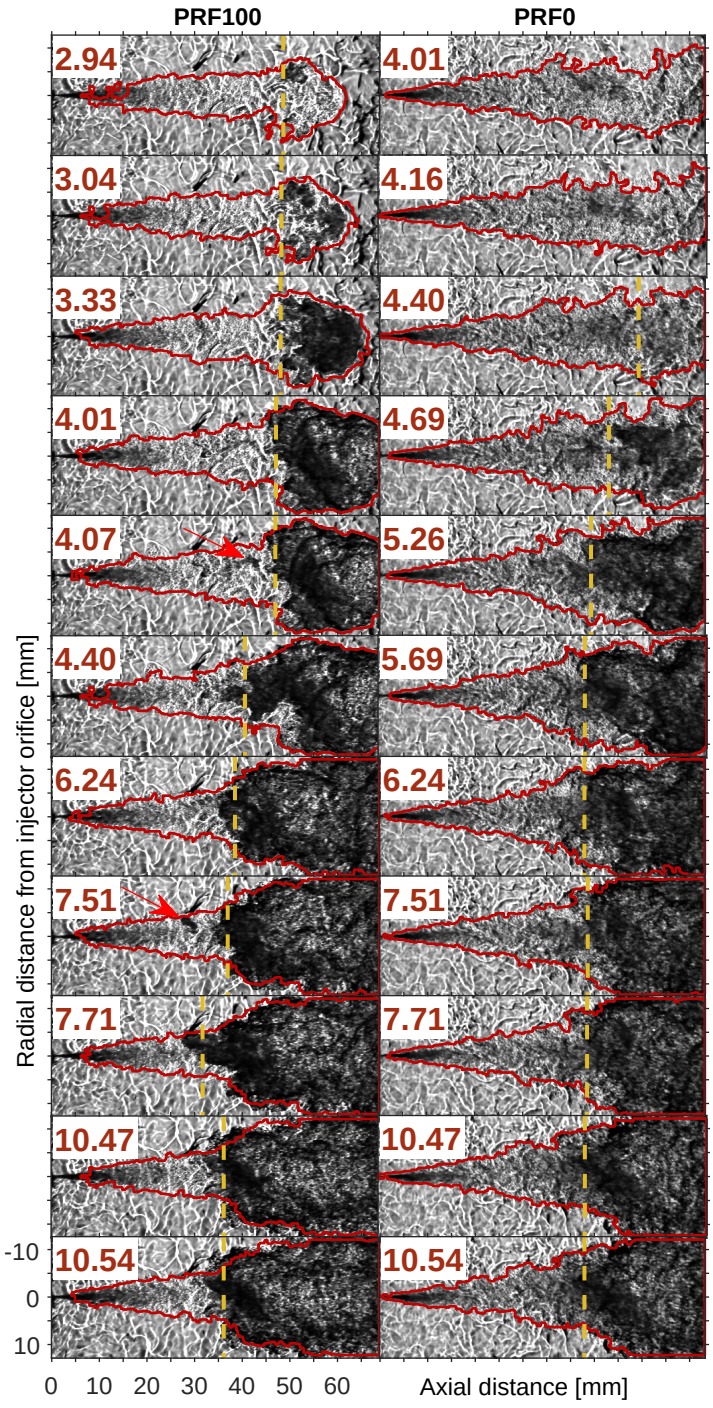

Figure 5: Typical time-resolved schlieren images for PRF100 (left) and PRF0 (right) without LI. Values at the top-left corners of the images indicate the time after start of injection (unit: ms aSOI). Yellow dashed lines indicate the instantaneous flame lift-off lengths that were derived by the method presented in Section 2.3.2. Red arrows indicate the darkened schlieren regions that are upstream and detached from the main flame body.

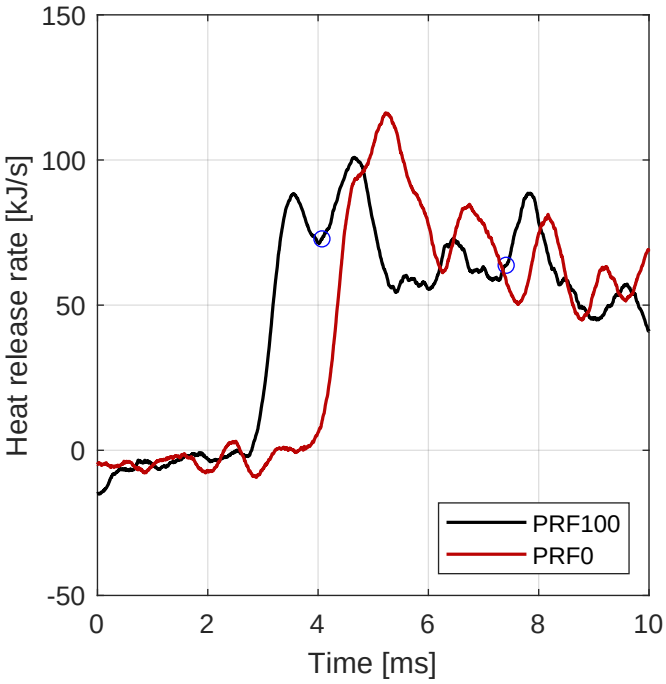

Figure 6: Heat release rate as a function of time (aSOI) for the PRF100 and PRF0 flames presented in Fig. 5. Solid black and red lines represent PRF100 and PRF0, respectively. Blue circles indicate the heat release rate at the time instants when the upstream isolated dark schlieren regions in Fig. 5 appear. For interpretations of the references to colour in this figure, the reader is referred to the web version of this article.

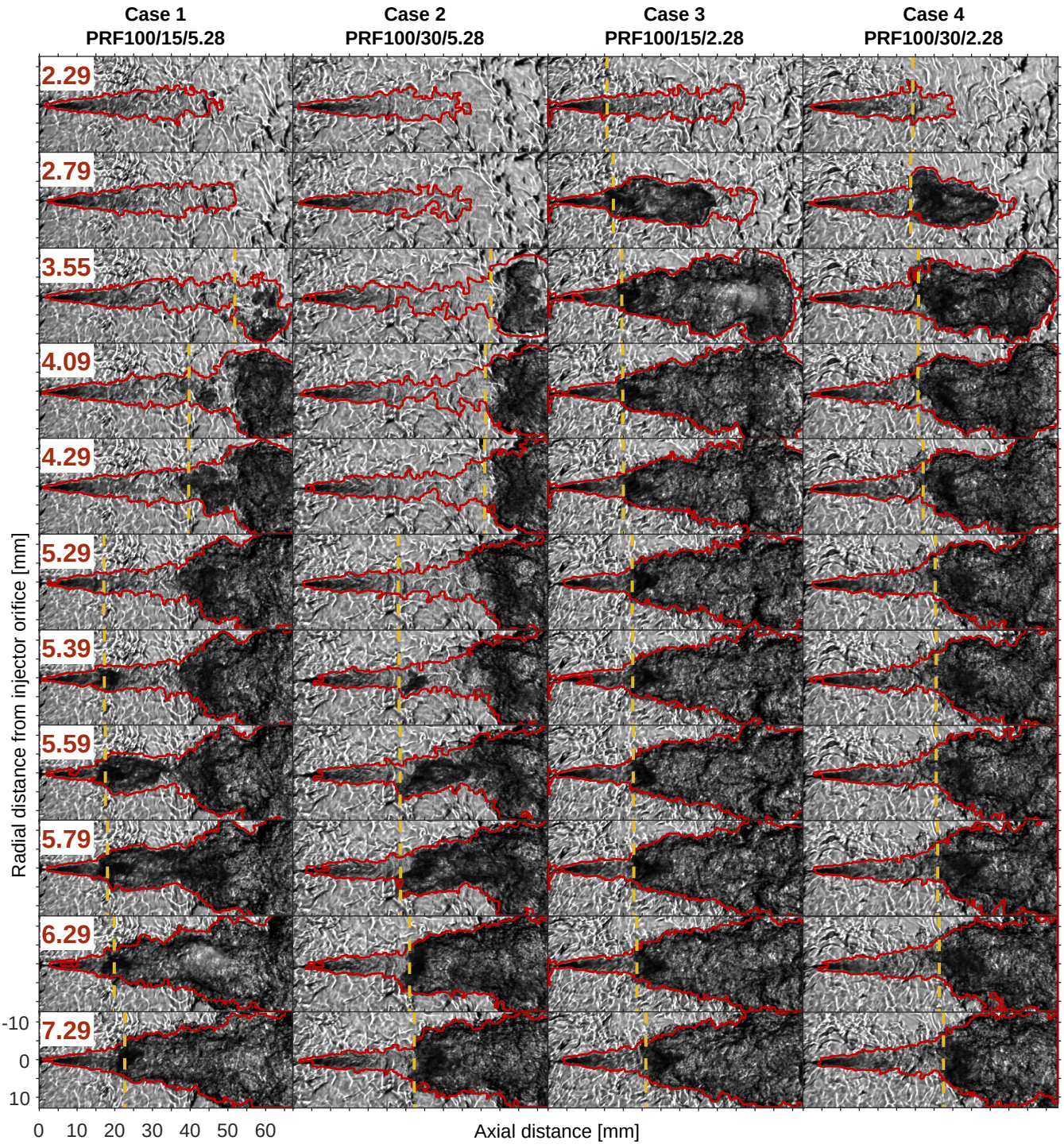

Figure 7: Typical time-resolved schlieren images for PRF100 cases with different LI locations and times. Each column represents one test case, which is indicated by the labels at the top of each column. Values at the top-left corners of the first column indicate the time after start of injection for each row of the images (unit: ms aSOI). Yellow dashed lines indicate the instantaneous flame lift-off lengths, as derived using the method presented in Section 2.3.2. Red crosses in the first row are used to indicate the focal points of LI for the test cases. Ambient conditions: 900 K, 22.8 kg/m^3, 21 vol.% O_2. Injection pressure: 70 MPa. Injection duration: 11.5 ms.

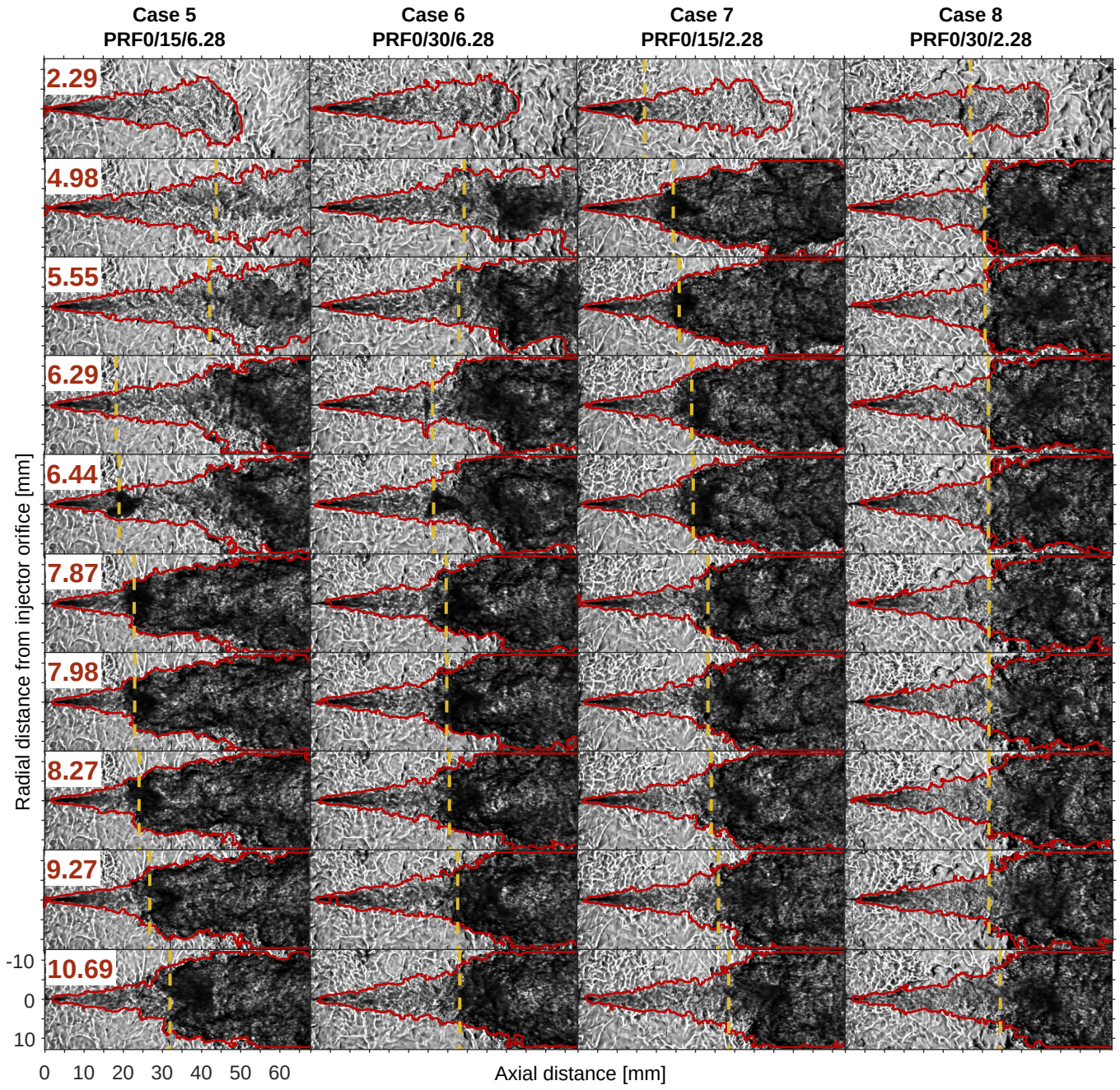

Figure 8: Typical time-resolved schlieren images for PRF0 cases with different LI locations and times. Each column represents one test case, which is indicated by the labels at the top of each column. Values at the top-left corners of the first column indicate the time after start of injection for each row of the images (unit: ms aSOI). Yellow dashed lines indicate the instantaneous flame lift-off lengths, as derived using the method presented in Section 2.3.2. Red crosses in the first row are used to indicate the focal points of LI for the test cases. Ambient conditions: 735 K, 22.8 kg/m^3, 21 vol.% O_2. Injection pressure: 70 MPa. Injection duration: 11.5 ms.

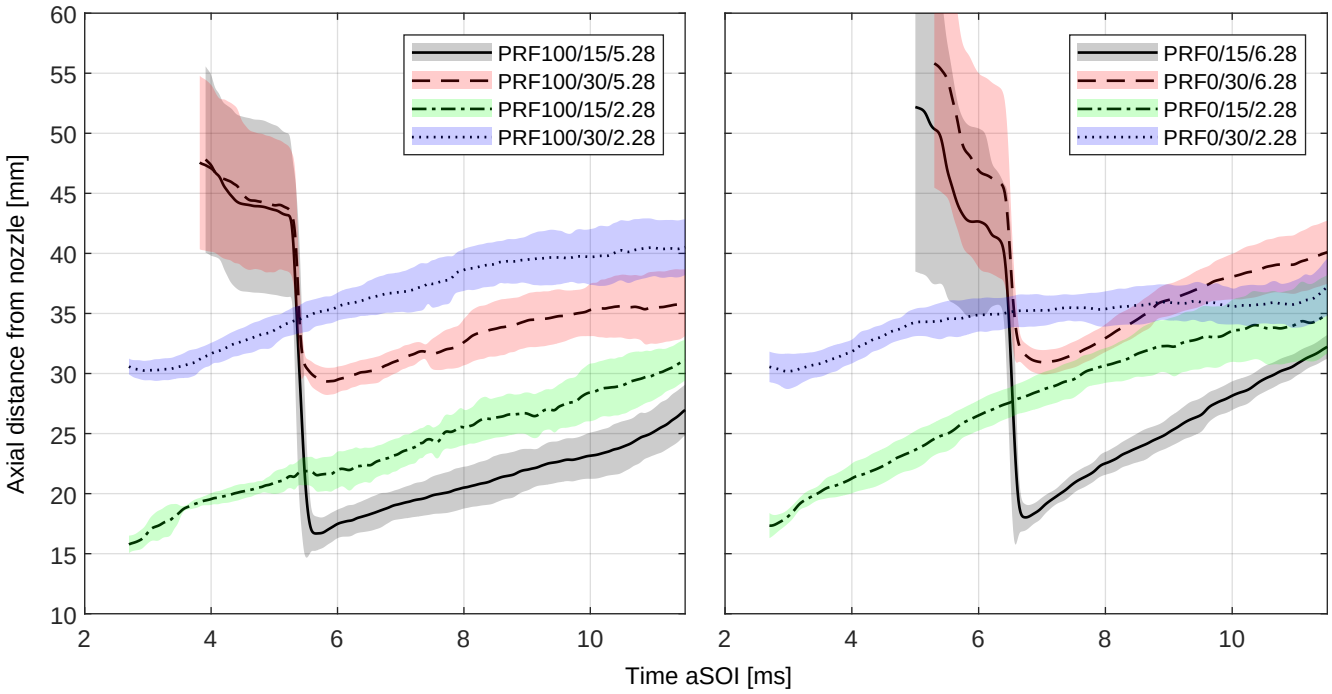

Figure 9: Ensemble-averaged instantaneous flame lift-off length traces for PRF100 (left) and PRF0 (right) at 8 test conditions. The names in legends provide information for the fuel/LI-location/LI-time-aSOI of the test cases. The colour shaded areas represent the associated run-to-run uncertainties (± 1 standard deviation). For interpretations of the references to colour in this figure, the reader is referred to the web version of this article.

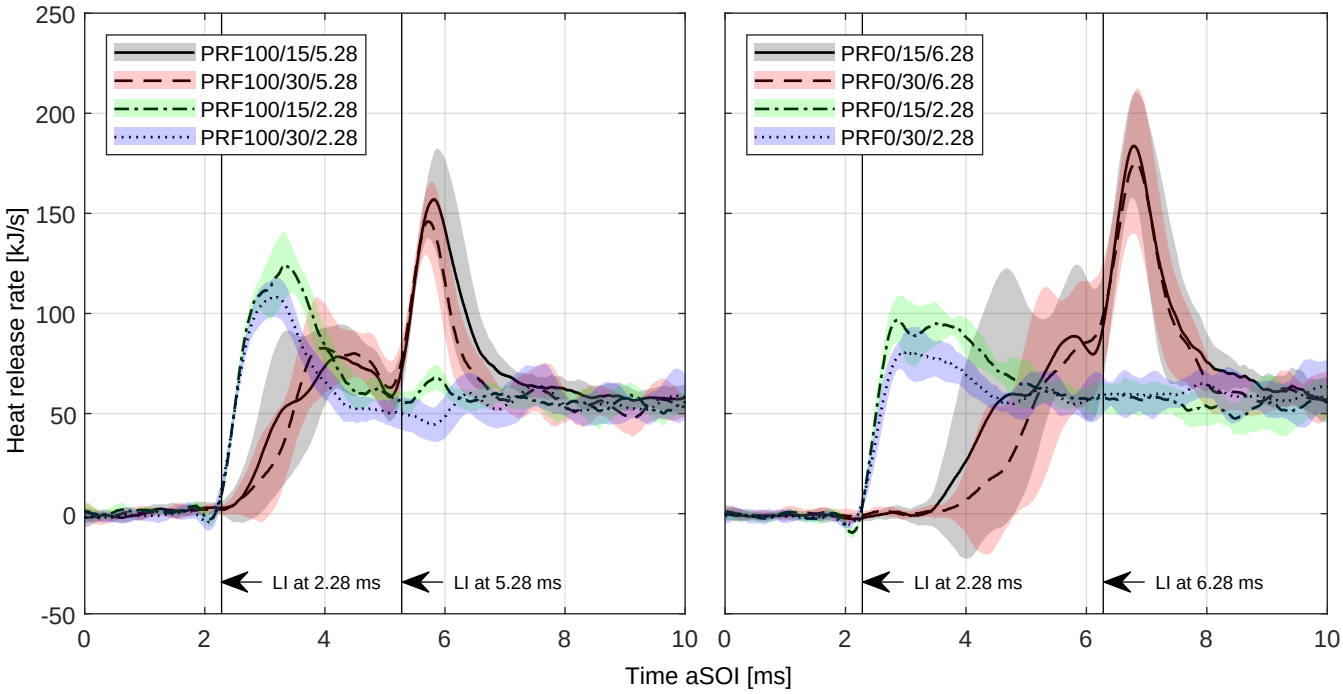

Figure 10: Ensemble-averaged HRR for the PRF100 (left) and PRF0 (right) jets at 8 different test conditions. The text descriptions in the legend provide the fuel/LI-location/LI-time-aSOI information for the test cases. The colour-shaded areas represent the run-to-run uncertainties (± 1 standard deviation). Vertically black solid lines, adjacent to black arrows, indicate the LI times. For interpretations of the references to colour in this figure, the reader is referred to the web version of this article.

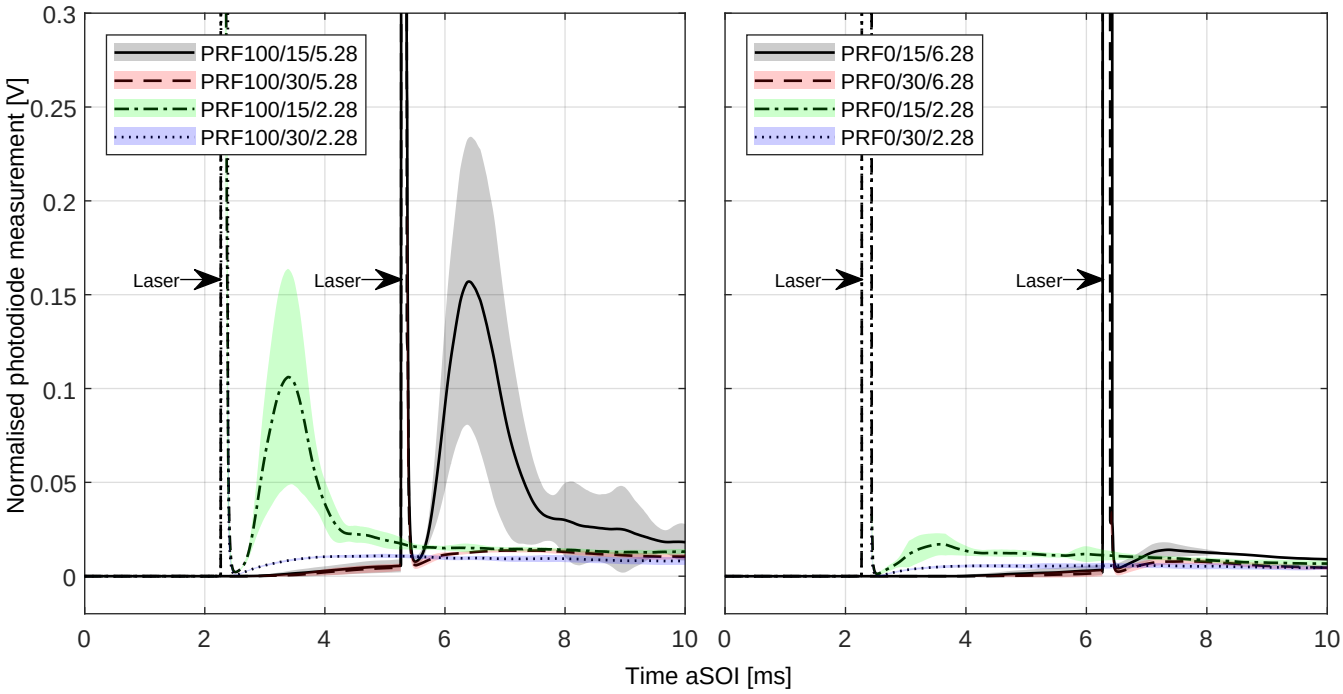

Figure 11: Ensemble-averaged photodiode intensity measurements for the PRF100 (left) and PRF0 (right) jets at 8 different test conditions. The text descriptions in the legend provides fuel/LI-location/LI-time-aSOI information for the test cases. The colour-shaded areas indicate the run-to-run uncertainties (± 1 standard deviation). For interpretations of the references to colour in this figure, the reader is referred to the web version of this article.

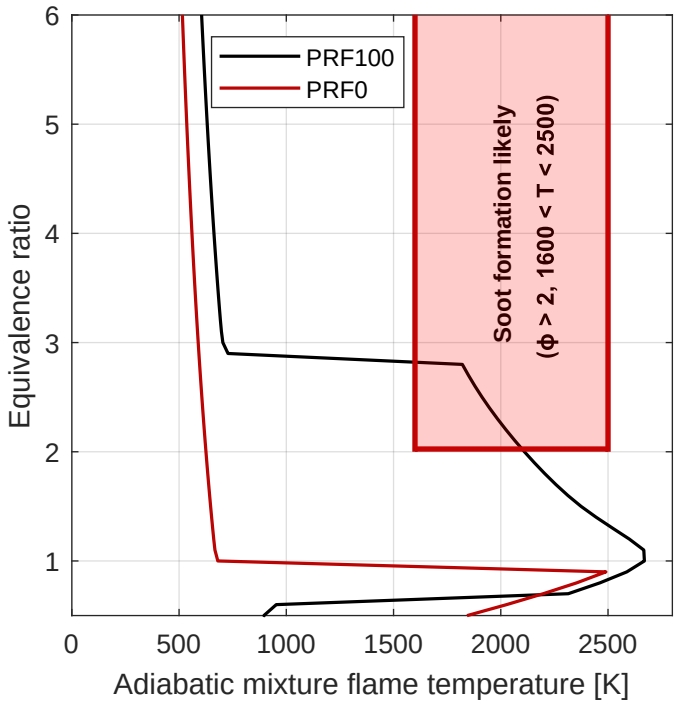

Figure 12: Adiabatic mixture flame temperature against equivalence ratio for PRF100 and PRF0 flames, when subjected to the test conditions of this work.